Applied Thermal Engineering 274 (2025) 126803

Contents lists available at ScienceDirect

Applied Thermal Engineering

journal homepage: www.elsevier.com/locate/apthermeng

Research Paper

Enhancement of thermal transport via electrostatic surface modification by ionic organic additives under electric fields: A molecular dynamics study

Haiyi Sun [a,b,*], Donatas Surblys [b], Taku Ohara [b]

[a] Department of Finemechanics, Graduate School of Engineering, Tohoku University, Sendai 980-8579, Japan
[b] Institute of Fluid Science, Tohoku University, Sendai 980-8577, Japan

ARTICLE INFO

Keywords:
Molecular dynamics
Interfacial heat transfer
Interfacial thermal resistance
Electric fields
Ionic organic additives

ABSTRACT

Enhancing interfacial heat transfer between graphite and polymers is crucial in modern technology. In this work, molecular dynamics simulations were conducted to study the heat transfer between graphite and polymers. Ionic organic additives (IOAs) were applied to enhance interfacial thermal transport under electric fields. IOAs are sodium dodecyl benzene sulfonate (SDBS) and dodecyl trimethyl ammonium bromide (DTAB). It was found that as the electric field strength increases, the interfacial thermal conductance increases. It was demonstrated that strong electric fields can dissociate IOAs and cause physical surface adsorption to enhance heat transfer. Adsorbed IOAs optimize vibration matching between graphite and polymers. Driven by electric field forces, IOAs migrate closer to the graphite interface, causing stronger repulsive van der Waals interactions and better transport of thermal energy. This study innovatively proposed a thermal management strategy, where electric fields cooperate with IOAs, expected to promote the development of electronic and energy equipment.

1. Introduction

With the development of modern technology, thermal processes are crucial in many fields, such as electronics and energy. Thermal issues can cause performance degradation and even safety incidents in electronic and energy equipment, urging for their efficient thermal management. As for the thermal management in the field of electronic, polymers act as the thermal interface materials to eliminate the interstitial air gaps between two contact surfaces inside electronic devices due to the softness and strong plasticity, promoting the heat dissipation [1,2]. Meanwhile, graphite possesses the high thermal conductivity, considered as the ideal thermally conductive filler to optimize the thermal properties of polymers [3,4]. However, the reported thermal conductivities of polymers with graphite-based fillers are often far below those predicted by theory because of the interfacial thermal resistance between graphite fillers and the polymer matrix [5–10]. In the energy field, polymers are used for electrolytes and separators of batteries, and graphite is a common electrode material. The bad thermal transport between graphite electrode and polymer electrolytes/separators can cause battery performance degradation or even thermal runaway [11]. All in all, it is of great significance to study and improve the interfacial heat transfer between polymers and the graphite, and thereby explore the novel thermal management strategies, which give rise to this study.

Many studies have investigated the enhancement of interfacial heat transfer between polymers and graphite. Ganguli et al. experimentally covalent-functionalized the graphite sheets with silane groups and demonstrated that silane functionalized graphite significantly decreases the graphite-polymer interfacial thermal resistance [12]. In addition, extensive molecular dynamics (MD) simulations have proven that covalent grafting of alkyl, formyl, carboxyl, amines, and hydroxyl functional groups onto graphite surfaces can efficiently enhance the heat transfer between the graphite and polymers [13–15]. Compared with covalent functionalization, noncovalent functionalization has the advantage of avoiding defects in the graphite plane and protecting its intrinsic thermal properties. Teng et al. conducted experiments to functionalize the single-layer graphite non-covalently using glycidyl methacrylate, and improved the heat transfer between graphite and polymers by 20.0 % [10]. Wang et al. performed MD simulations to calculate the interfacial thermal resistance between the single-layer graphite and polymers using a noncovalent functionalization of localized pyrene groups. They attributed the improved heat transfer to vibrational matching between the single-layer graphite and non-covalently modified molecules [16]. However, noncovalent functionalization of the graphite does not improve heat transfer as much as

---

* Corresponding author.
E-mail address: sun.haiyi.s1@dc.tohoku.ac.jp (H. Sun).

https://doi.org/10.1016/j.applthermaleng.2025.126803
Received 10 June 2024; Received in revised form 23 April 2025; Accepted 10 May 2025

covalent functionalization and its stability is usually weaker than that of the covalent functionalization. In summary, the existing technologies for improving heat transfer between graphite and polymers have shortcomings, urging for more research.

In actual application scenarios, heat transfer between the graphite and polymers often occurs under an electric field. For example, an electric field is generated internally when electronic devices operate and also appears inside the electrodes of batteries when they are charging or discharging. In some laboratories, the application of an external electric field on the order of $0.1 - 1.0$ V Å^{-1} has been realized via scanning tunneling microscopy and atomic force microscopy [17,18], which means regulating thermal transport by electric fields is technically achievable. Although the study of heat transfer enhancement by electric field has existed such as the enhanced boiling heat transfer and nanofluidic heat transfer [19,20], the explanation of the related heat transfer mechanism is still insufficient and needs more research. Molecular dynamics methods are widely applied to understand heat transfer mechanisms at the atomic perspective exhibiting great potential [21–24]. In fact, there has been some progress in studying heat transfer under electric fields via MD methods. Conducting MD simulations, Ma et al. applied an electric field near the graphite surface to induce ordered water layers and improve interfacial thermal conductance (ITC) [25]. Song et al. investigated the mechanism of the enhanced thermal conductivity of aramid polymers induced by electric fields using MD simulations [26]. These studies inspired researchers to utilize the external electric fields to optimize the heat transfer and extending electric fields to optimize heat transfer in more and realistic fields is meaningful, which acted as an inspiration for this work to enhance heat transfer between graphite and polymers.

In this work, the use of electrostatic surface modification by ionic organic additives (IOAs) under electric fields of $0.1 - 3.0$ V Å^{-1} to enhance thermal transport over the interface between graphite and polymers was investigated via molecular dynamics simulations. Polyethylene (PE) was selected as the matrix of polymers. The IOAs applied are sodium dodecyl benzene sulfonate (SDBS) and dodecyl trimethyl ammonium bromide (DTAB). For brevity, polyethylene without and with IOAs are respectively named "pure polymer" and "composite polymer" in this work. First, ITC between the graphite and pure/composite polymers is evaluated to estimate heat transfer performance under different electric fields. Then, the effect of electric fields on the distribution of IOAs is studied. In addition, the effect of electric field strength on interfacial potential energy is also investigated. Lastly, vibration density of states (vDOS) and ITC decompositions according to various contributions from interaction forces across the interface are studied to elucidate the underlying heat transfer mechanism.

Our group has previously reported that the heat transfer between polymer and silica can be enhanced by adding several organic additives to the polymer [27,28]. This work can be considered as the extension of our previous original work, where organic additives are explored to cooperate with electric fields to improve the heat transfer between graphite and polymers. To our best knowledge, no research has proposed a similar strategy to enhance heat transfer between polymer and graphite before. Given the importance of heat transfer between graphite and polymer in practical applications, this research is meaningful for improving thermal management of electronic and energy devices. Moreover, this study conducted molecular dynamics method to uncover the underlying physical mechanism of electric field enhanced heat transfer from the view of molecular nanoscale level, which is a good supplement to the existing knowledge of the effect of electric fields on heat transfer.

2. Simulation details

2.1. Simulation system

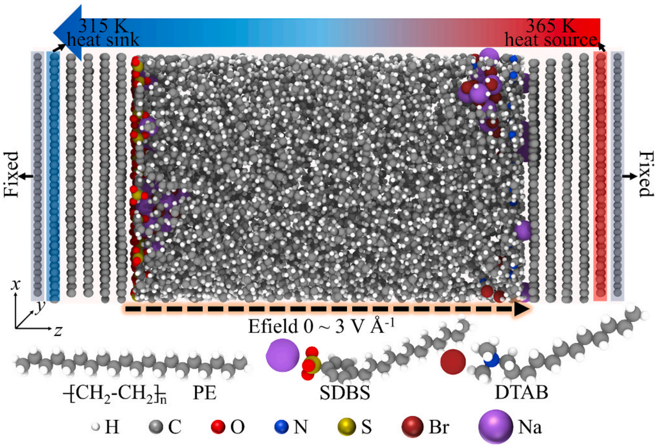

Fig. 1. Schematic of the simulation system, as well as the polyethylene (PE), sodium dodecyl benzene sulfonate (SDBS) and dodecyl trimethyl ammonium bromide (DTAB). SDBS and DTAB are ionic organic additives, added into PE at the PE-graphite interface.

As shown in Fig. 1, pure/composite polymers are sandwiched between two graphite walls along the z direction. The graphite wall on each side consists of six single-layer graphite sheets spaced 3.4 Å apart. The size of each single-layer graphite slice is 45.5 (x) × 43.8 (y) Å^2, constructed from 720 carbon atoms. Each single-layer graphite slice has zigzag orientation and armchair orientation in the x and y directions. The PE is selected as the pure polymer. The PE model in this work is formed by single chain polyethylene without cross-linked or branched structures, which has been applied in previous MD simulations [29,30]. Composite polymers are obtained by adding two types of ionic organic additives into PE, which are SDBS and DTAB. As shown in Fig. 1, through mutual electrostatic attractions of ionic pairs, one SDBS molecule is composed of a negatively charged dodecyl benzene sulfonate ion (DBS$^-$) and a sodium ion (Na$^+$), and one DTAB molecule is composed of a positively charged dodecyl trimethyl ammonium ion (DTA$^+$) and a bromine ion (Br$^-$). In this work, the molecule numbers of PE, SDBS, and DTAB are respectively 168, 36 and 36. 168 chains of PE molecules contain 3192 repeat units of methylene, comparable to the polymer systems in the work of Tian et al. [31]. The 36 chains of SDBS and DTAB correspond to 15.0 % mole fraction of additives, in the range of the work of Guo et al. (5.0 % – 20.0 %) [28]. Each simulation system is kept at pressure of 1.0 atm using the pressure control method introduced in a later paragraph, and the system sizes of graphite-pure polymers and graphite-composite polymers are respectively 89.7 Å and 110.7 Å along the z direction. In Section S1 of the Supporting Information, a relevant discussion on the size effect of simulation boxed is given to convince our simulation box size is available.

2.2. Simulation setup

All MD simulations were performed by the large-scale atomic/molecular massively parallel simulator (LAMMPS) [32] with a 0.5 fs timestep. Time integration algorithm of velocity Verlet was used [33]. The open visualization tool (OVITO) was used for model visualization [34]. For the graphite walls, interactions of intralayer carbon atoms were modeled with the Tersoff potential [35], and interactions of interlayer carbon atoms were modeled by the 12–6 Lennard-Jones (LJ) potential with parameters from the work of Girifalco et al. [36]. The all-atom optimized potentials for liquid simulation (OPLS-AA) force field was selected to model the organic liquid polymers (i.e., PE, SDBS, and DTAB), where the parameters of Na$^+$ and Br$^-$ were adapted from the revised OPLS-2009IL force field [37,38]. All organic liquid polymers were constructed using the LigParGen web portal [39], which provides the atomic charge of PE, SDBS, and DTAB molecules based on the OPLS-AA force field. These atomic charges of PE, SDBS, and DTAB molecules have been widely used to study the heat transport of organic liquids [40,41]. Intermolecular interactions between dissimilar m-th and n-th atoms were calculated using the 12–6 LJ potential and the parameters were obtained by the geometric mixing rule: $\varepsilon_{mn} = \sqrt{\varepsilon_m \varepsilon_n}$ and $\sigma_{mn} = \sqrt{\sigma_m \sigma_n}$. The LAMMPS data file of our simulation system is included in the Supplementary Material to provide complete force field parameters. In addition, electric fields of 0 to 3.0 V Å^{-1} were applied to the organic liquid polymers. This was done by exerting an external force on each charged atom, according to:

$$F_{\text{efield}} = qE_{\text{strength}} \tag{1}$$

where F_{efield} is the electric field force,q is the atomic charge, and E_{strength} represents the electric field strength. In the x and y directions, the simulation system was periodic, while the z direction was non-periodic. Simulations set the cut-off radius of all short-range interactions as 12.0 Å. In addition, the long-range Coulombic interactions were computed by a modified particle–particle particle–mesh (PPPM) algorithm with an accuracy of 1×10^{-6}, while also taking into account that the simulation system is not periodic in the z direction [42,43].

2.3. Simulation procedures

The overall MD simulation procedures for each simulation case consist of three phases: the initial preparation (50.0 ns), the dynamic equilibration phase (25.0 ns), and the data sampling (20.0 ns).

At the initial preparation phase, different bulk components were assembled in the special order of the graphite wall, SDBS, PE, DTAB, and the graphite wall (from left to right). SDBS and DTAB are ionic organic additives, added into PE at the PE-graphite interface. In addition, a simulation system constructed by sandwiching pure PE between two graphite walls was built to compare to the above systems with the aim of clarifying the effect of adding IOAs on the interfacial heat transfer. The dimensions of each bulk component in the x and y directions were respectively 45.5 Å and 43.8 Å. The initial dimensions of the graphite walls, SDBS, PE, and DTAB in the z direction were around 17.0 Å, 30.0 Å, 50.0 Å and 25.0 Å. To eliminate the initial pseudo-crystal structure of these organic liquid polymers (i.e., SDBS, PE, and DTAB) and blend all independent components, the whole system was first relaxed under 600.0 K for 50 ns using the Nosé–Hoover thermostat with a damping coefficient of 50.0 fs, where two outmost single-layer graphite sheets of the graphite walls on the left and right sides were fixed. The number of the Nosé–Hoover thermostat chain was 3.0 [44], and the equation of motion contained the correction terms from Martyna, Tuckerman, and Klein [45].

In the second phase, a nonequilibrium molecular dynamics simulation (NEMD) was performed in two steps. In the first step, the leftmost single-layer graphite sheet of the graphite walls was kept fixed while an external force was applied to the rightmost single-layer graphite sheet of the graphite walls in the z direction on each carbon atom to control the system pressure at 1.0 atm. Meanwhile, as shown in Fig. 1, two second-outermost single-layer graphite sheets of the graphite walls on the left and right sides respectively acted as a heat sink and heat source at 315.0 K and 365.0 K, using Langevin thermostats with a damping coefficient of 50.0 fs. These temperature settings of heat sink and heat source are consistent with previous work [27,28] and cover common operating temperatures for batteries and electronic devices [11,46–48]. This phase aimed to generate a stable heat flux, realize a relatively linear temperature gradient, and acquire a system pressure of 1 atm. The first step lasted for 20.0 ns, where the oscillating position of the rightmost single-layer graphite sheet of the graphite wall was recorded, and the final position of the rightmost single-layer graphite sheet of the graphite wall was determined by averaging the position data of the last 10.0 ns. Afterwards, in the second step, the rightmost single-layer graphite sheet of the graphite wall was fixed at its average position, and diverse electric fields of 0 to 3.0 V Å^{-1} were applied, affecting only the organic liquid polymers because the carbon atoms of the graphite walls were neutral. The second step continued with another 5.0 ns to eventually acquire a stable non-equilibrium system. In Section S2 of the Supporting Information, the proper energy balance of this quasi-equilibrium phase was shown.

At the third and final data sampling phase, simulation continued for 20.0 ns to conduct data sampling, obtaining various system properties such as atomic position and temperature distribution. Basically, the temperature is calculated via Eq. (2):

$$T = \frac{1}{3Nk_B} \sum_{i=1}^{N} m_i {v_i}^2 \tag{2}$$

where N is the number of atoms in a specific group, k_B is the Boltzmann constant, i is the atom index, and m and v are mass and velocity. Each single-layer graphite sheet of the graphite walls is considered as a group to calculate its temperature using Eq. (2). To mark the position of each single-layer graphite sheet of the graphite walls in the z direction, the position value of z dimension for each carbon atom in the single-layer graphite sheet of the graphite walls is averaged. To describe the temperature distribution of polymers along the z direction, simulation region locating polymers is divided into several chunks along the z direction, where each chunk is with the size of 45.5 (x) × 43.8 (y) × 0.5 (z) Å^3. Polymer atoms in each chunk are considered as a collection to represent the local polymer temperature using Eq. (2) and the geometric center of each chunk in the z direction marks its position, realizing the description of the polymer temperature distribution along the z direction. These position and temperature information are outputted once every 50.0 fs and the final position and temperature are obtained by averaging all data during the whole sampling process of the total 20.0 ns. The standard error was calculated by dividing data into 10 blocks to estimate the uncertainty of results [49]. In Sections S3 – S5 of the Supporting Information, the temperature, pressure, and energy data of this phase were reported.

3. Results and discussion

3.1. Interfacial thermal conductance

Interfacial thermal conductance is obtained according to Eq. (3):

$$ITC = \frac{Q_z}{A\Delta T} \tag{3}$$

where Q_z is the heat flow in the z direction acquired from computing the energy input and output rate of two Langevin thermostats in the heat sink and heat source, A is the cross-section area of the x-y plane, and ΔT is the temperature jump at the interface caused by interfacial thermal resistance. Fig. 2(a) illustrates the calculation of ΔT, which is defined as the temperature difference between the interfacial single-layer graphite sheet of the graphite walls and organic liquids. The solid–liquid interface position is defined as the position of the innermost single-layer graphite sheet of the graphite walls, whose temperature is considered as the interfacial solid temperature. The temperature of the organic liquid polymers at the interface can be obtained by linearly fitting and extrapolating the temperature curves of organic liquid polymers from the area further than 20 Å from the position of the solid–liquid interface. Generally, there is no fixed standard for the selection of the region for linearly fitting and extrapolating the liquid temperature to the interface. As our previous work reported [50], for long-chain polymer liquids, it is more advantageous to use the near-wall temperature curve to fit and extrapolate the interfacial liquid temperature, because it can better reflect the effect of the dynamic behaviors of the interfacial liquids on heat transfer. In fact, some previous works have also selected the liquid temperature near the interface for fitting and extrapolation [51,52], which is similar with our choice. Fig. 2(b) displays the heat source and sink energies extracted from Langevin thermostats versus simulation

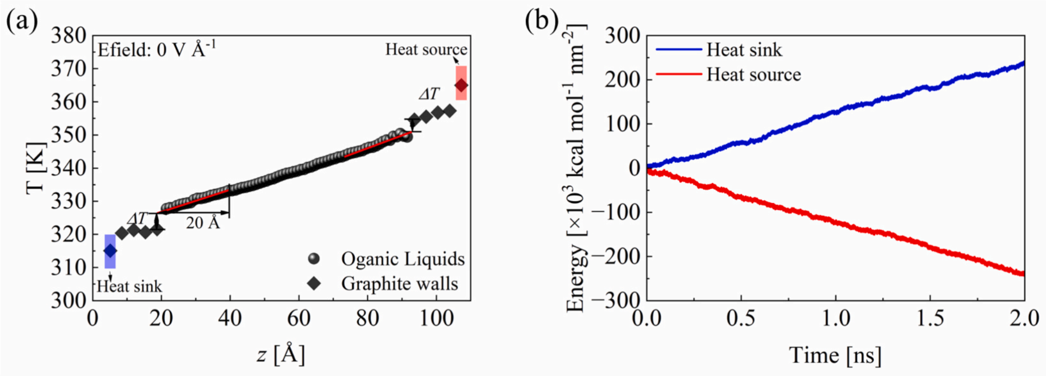

Fig. 2. (a) Temperature distribution of the graphite-composite polymer system without the electric field; (b) Heat source and sink energies extracted from Langevin thermostats versus simulation time for the graphite-composite polymer system without the electric field. The temperature of the fixed layers should be 0 K due to the atomic stillness.

time from which Q_z can be calculated.

Fig. 3 displays the ITC results. As we can see from Fig. 3, when there is not an electric field, ITC between the graphite walls and pure polymers are respectively 179.1 ± 24.0 MW K^{-1} m^{-2} and 170.3 ± 24.0 MW K^{-1} m^{-2} on the cold and hot sides. Adding IOAs into the PE matrix, graphite-composite polymer system reports ITCs of 154.2 ± 8.1 MW K^{-1} m^{-2} and 149.4 ± 27.0 MW K^{-1} m^{-2} on the cold and hot sides when an electric field is not employed. Such ITC values are consistent with ITC of about 150 MW K^{-1} m^{-2} in the work of Wang et al. [15], where interfacial heat transfer between graphite and paraffin was studied. Based on the temperature distribution of graphite-pure polymer system, the thermal conductivity of PE can be calculated by substituting the temperature gradient of bulk PE molecules into the ΔT term of Eq. (3). The thermal conductivity of PE is 0.2 W K^{-1} m^{-1} in this work, consistent with the reported experimental values of 0.2 W K^{-1} m^{-1} [53,54]. These results validate of our simulation results. After only adding IOAs, ITC respectively decreases by 14.0 % and 12.4 % at the cold and hot sides. This result may be due to the difference in molecular structure between IOAs and PE, which leads to IOAs occupy larger space than PE molecules at the interface. We counted the total number of atoms in the region 12.0 Å away from the interface. For graphite-pure PE systems, there are about 2441 and 2322 atoms at the cold and hot sides. However, after IOAs are added into the PE at the interface, there are about 2045 and 1932 atoms at the cold and hot sides. Fewer interfacial atoms lead to larger nanoscale voids, resulting in the slight drops in ITC values after adding IOAs into the PE. Considering the uncertainty of the calculated ITC values evaluated by the standard error, 14.0 % and 12.4 % decrease in ITCs at the cold and hot sides may not be a deterministic interface heat transfer degradation because the decrease in ITC values caused by the added IOAs are within the error range. This work prefers not to regarding this decrease in values as an important and fixed conclusion. On the other hand, though the distribution or concentration of SDBS and DTAB at the interface of the composite polymer is possible to influence ITC to some extent, this effect should not be large enough because PE, SDBS and DTAB have the same framework of alkyl which is the main molecular component, especially compared to the effect of electric fields which is our focus (Fig. 3).

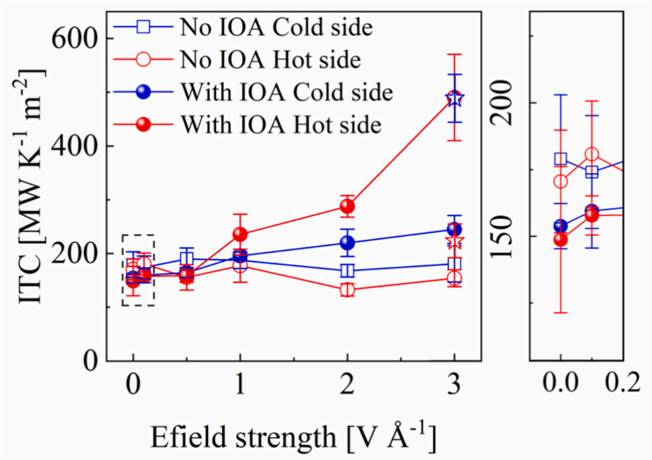

Fig. 3. Variations of ITC as electric field strength increases for graphite-pure polymer and graphite-composite polymer systems. The blue and red pentagrams represent the ITCs on the cold and hot sides when the heat source and heat sink is reversed under the electric field of 3.0 V Å^{-1}. The inset on the right is a zoom-in image of ITC results under the electric fields of 0 and 0.1 V Å^{-1}.

As shown in Fig. 3, if IOAs are not added while applying an electric field, ITC is almost constant as the electric field strength increases, which demonstrates that the electric field has little effect on the heat transfer between graphite and PE. This is expected since PE molecules are electrically neutral. What needs to be stated is that the ITC values calculated according to Eq. (3) can vary at different sampling periods because of the linear extrapolation method for obtaining interface temperature and the numerical statistics of the simulation results. Moreover, we point out that though PE is electrically neutral, parts of their molecules are non-neutral, which can induce the heat transfer conditions of the system to fluctuate as well as the ITC fluctuation. According to the uncertainty of ITC values evaluated by the error bar showing in Fig. 3, these value fluctuations can be considered that the electric field has no effect on heat transfer.

We investigate the ITC variations of composite polymer systems under external electric fields. Initially, for the composite polymer systems containing IOAs, ITC can be relatively constant if the electric field is weak ($E_{\text{strength}} \leq 0.1$ V Å^{-1}). However, when the electric field strength is larger (0.5 – 3.0 V Å^{-1}), ITC significantly increases, demonstrating that a cooperation between electric fields and IOAs can be beneficial to interfacial heat transfer. Generally, ITC on the hot side is larger, as shown in Fig. 3. Specifically, when the electric field strength is heightened to 3.0 V Å^{-1}, ITC is respectively increased by 60.2 % and 230.3 % on the cold and hot sides, respectively. To demonstrate if such different degrees of ITC enhancement are caused by the temperature effect, we conducted an extra simulation, where the positions of the heat source and heat were reversed, and we performed the same simulation procedures as described in Section 2.3. In Fig. 3, blue and red pentagrams represent the ITCs of this extra simulation on the cold and hot sides. In this extra simulation, ITCs are 213.3 ± 31.1 MW K^{-1} m^{-2} and 488.4 ± 44.6 MW K^{-1} m^{-2} on the hot and cold sides, which are similar with the ITCs of 245.1 ± 26.5 MW K^{-1} m^{-2} and 490.8 ± 80.7 MW K^{-1} m^{-2} on the cold and hot sides in the origin simulations. Therefore, the effect of the interfacial temperature on ITC can be negligible. In other words, the different degrees of ITC enhancement are due to the surface modification of distinct IOAs (i.e., SDBS and DTAB) under the electric fields rather than the temperature effect.

3.2. *Effect of electric fields on the distribution of ionic organic additives*

As discovered in Section 3.1, independently adding IOAs without applying external electric fields does not significantly enhance the interfacial heat transfer. Thereby, the electric field is thought to affect the distribution of IOAs and enhance heat transfer. Through mutual electrostatic attractions of ionic pairs, SDBS is constructed from DBS^- and Na^+ ions, and DTAB is made up of DTA^+ and Br^- ions. Here, effects of electric fields on the distribution of IOAs are first clarified by studying the position of these four components via the radial distribution functions (RDF).

Fig. 4(a) and (b) respectively display the RDF of Na^+ and Br^- around DBS^- and DTA^+, where sulfur (S) and nitrogen (N) atoms mark the DBS^- and DTA^+. When there is no electric field, Na^+ and Br^- tightly couple with DBS^- and DTA^+. Even if the E_{strength} is slightly enhanced to 0.1 V $Å^{-1}$, these two ionic pairs (i.e., Na^+DBS^- and DTA^+Br^-) can remain bonded, and thereby the RDF profiles do not significantly change. However, as the E_{strength} gets higher ($\geq$0.5 V $Å^{-1}$), some SDBS and DTAB molecules begin to dissociate into two components with positive and negative charges (i.e., Na^+/DBS^- and DTA^+/Br^-). This causes some Na^+ and Br^- ions to no longer coordinate with DBS^- and DTA^+ ions. As a result, the highest RDF peaks in Fig. 4(a) and (b) become duller as the electric field strength becomes larger than 0.1 V $Å^{-1}$. This suggests that the electric field forces act to separate ionic pairs in the SDBS or DTAB molecules, and once the electric field force is large enough to overcome the electrostatic attractions of these ionic pairs, IOAs are dissociated into two ionic components. In such a case, the dissociated Na^+ and Br^- move freely and their amount around DBS^- and DTA^+ decreases, as displayed in Fig. 4(a) and (b). As the electric field strength increases, the highest peaks of RDF in Fig. 4(a) and (b) decrease, indicating more IOAs are dissociated. Subsequently, once the IOAs are dissociated, Br^- and DBS^- can migrate towards the cold side, and Na^+ and DTA^+ can transport towards the hot side driven by the electric field forces in our simulation system. Thus, the graphite surfaces on the cold side are modified by DBS^-, and graphite wall surfaces on the hot side are modified by DTA^+, which can be considered similar with the surface modification using surfactants [27,28].

Fig. 4(c) and (d) depict the RDF of DBS^- and DTA^+ ions around the graphite surfaces, where sulfur and nitrogen atoms respectively belong to DBS^- and DTA^+. When E_{strength} is 0 or 0.1 V $Å^{-1}$, RDF does not exhibit any clear peaks or valleys, which means that the long-chain DBS^- and DTA^+ ions do not form a relatively fixed coordination relationship with the graphite walls and are adsorbed on the graphite wall surfaces. This is easy to explain. As DBS^- and DTA^+ couple with the corresponding counter ions (i.e., Na^+ and Br^-) in such cases, and thereby they are not significantly driven by the electric field force because IOAs are not dissociated. As the electric field strength increases, RDF exhibits clearer peaks, indicating that DBS^- and DTA^+ ions do form relatively stable coordination structures on the graphite surface. In such cases, the long-chain ions of DBS^- and DTA^+ are pressed and confined on the graphite surface by the electric field forces. The configurations of DBS^- and DTA^+ on graphite surfaces are similar to the surfactants adsorbed on the silica surfaces via hydrogen bonds [27,28] or the self-assembled monolayers (SAMs) modifying solid surfaces by covalent bonds [55].

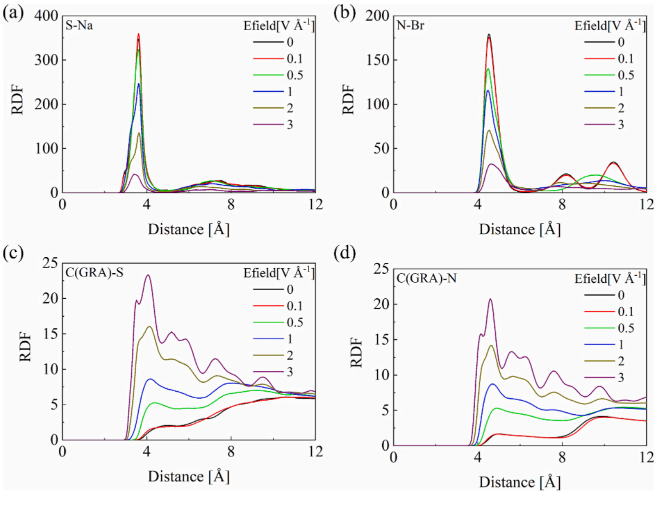

Fig. 4. (a) The RDF of Na^+ around DBS^-; (b) the RDF of Br^- around DTA^+; (c) the RDF of DBS^- around the graphite surface; (d) the RDF of DTA^+ around the graphite surface. The sulfur (S) and nitrogen (N) atoms are used to respectively denote DBS^- and DTA^+.

In a SDBS molecule, there is a benzene ring, which has a similar structure with the a single-layer graphite sheet of the graphite walls. Interestingly, we observe the orientation variations of benzene rings as the E_{strength} increases, as shown in Fig. 5(a). Here, we study the orientation distribution of benzene rings of SDBS. As shown in Fig. 5(b), the angle between the direction vector formed by the two carbon atoms of a benzene ring and the *z*-axis is used to represent the benzene ring orientation. An angle of zero degree means that a benzene ring orients perpendicularly to the graphite surface and an angle of ninety degrees means that a benzene ring has an orientation parallel to the graphite surface. In Fig. 5(b), if the electric field was not applied, the orientation of benzene rings is mostly random with angles of 40.0°–90.0°, which is consistent with the snapshot in Fig. 5(a). As we can see from Fig. 5(b), benzene rings exhibit the specific orientation when an electric field was applied, that is benzene rings tend to be either parallel or vertical to the graphite surfaces. On the one hand, an electric field force can induce the benzene ring to orient parallel to the direction of electric field, which has been reported by the previous work [56]. On the other hand, as the E_{strength} increases to 3.0 V $Å^{-1}$, SDBS molecules start to dissociate and the dissociated DBS^- ions can migrate towards the graphite surfaces, and hence these benzene rings exhibit parallel orientation towards the graphite surface in the vicinity of the interfaces. Such phenomena is somewhat similar to the π-π stacking images on the graphite wall surfaces [57,58], which is expected to be a more stable adsorption structures of DBS^- on the graphite wall surfaces, and bridge the heat path at the interface discussed in the later sections. Fig. 5(a) supports this as well.

3.3. *Analysis of interfacial potential energy*

As discussed in Section 3.2, electric fields can influence the distribution of IOAs on the graphite surfaces, which is expected to affect the interfacial potential energy between the graphite walls and organic liquid polymers. As shown in Fig. 6, interfacial potential energy on the cold side is smaller than that on the hot side. This is because liquid density is higher on the cold side promoting more liquid atoms to interact with the solid, as reported by previous works [50,59]. We can also readily observe that even though E_{strength} becomes larger, the interfacial potential energy does not change significantly for graphite-pure polymer systems without IOAs, demonstrating that electric fields do not enhance the interactions between the graphite wall and PE. This is expected because the PE is electrically neutral.

On the other hand, compared to graphite-pure polymer systems, interfacial potential energy of the composite polymer systems finally increases when electric fields are applied though the interfacial potential energy at the cold side for the graphite-composite polymer system decreases from $-$ 437.5 kcal mol^{-1} nm^{-2} to $-$ 455.5 kcal mol^{-1} nm^{-2} as the electric field strength increases from 0.1 V $Å^{-1}$ to 1.0 V $Å^{-1}$, which is about 4.0 % decrease. For the graphite-composite polymer systems, as

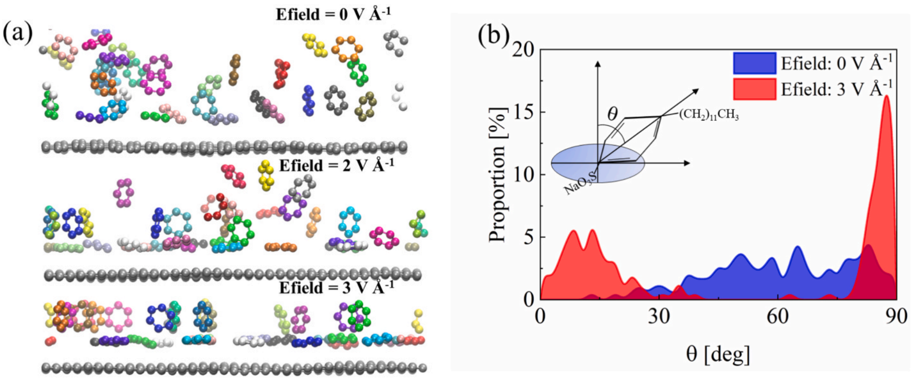

Fig. 5. (a) The snapshots to display the orientation variation of benzene rings of SDBS as the electric field strength increases. (b) Orientation distribution of benzene rings of SDBS under electric fields of 0 and 3.0 V $Å^{-1}$.

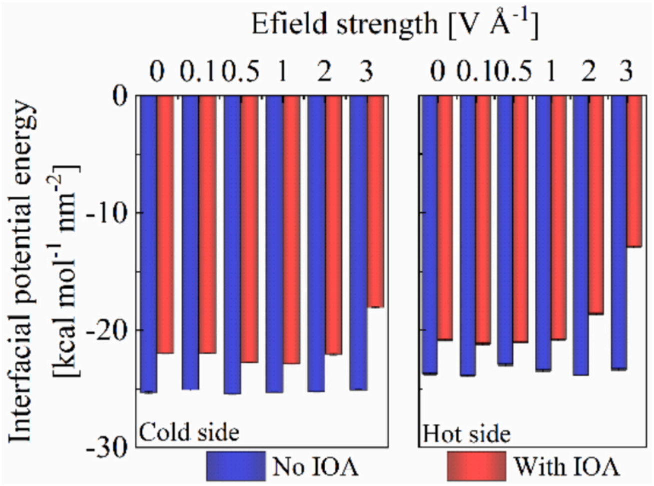

Fig. 6. Variations of interfacial potential energy as electric field strength increases for graphite-pure polymer and graphite-composite polymer systems.

the electric field strength increases from 0.1 V $Å^{-1}$ to 1.0 V $Å^{-1}$, IOAs start to dissociate into two ionic components, causing the changes in the composition, structure and dynamic behaviors of the interfacial liquids under the electric fields, which affects the interfacial potential energy. For example, as the dissociation happens, Na^+ moves away from the cold side while Br^- migrates towards the cold side. In our work, the interactions between graphite and Br^- are stronger than Na^+, and hence the interfacial potential energy should possibly decrease. In addition, Br^- is easier to transport in the polymers than Na^+ [60,61]. As a result, more Br^- can gather at the cold side if Na^+ is trapped in the polymers when it transfers, leading to a decrease in the interfacial potential energy. In my opinion, this 4 % decrease is generally difficult to explain quantitatively and exactly because the composition, structure, and dynamic behavior of the interfacial liquid are complex, which need more research in the future work. Generally, smaller interfacial potential energy (i.e. the larger absolute values of the interfacial potential energy) denotes stronger solid–liquid interactions, and thereby superior interfacial heat transfer performance [55,62]. As the electric field strength slightly increases ($\leq$0.1 V $Å^{-1}$), interfacial potential energy is almost unchanged for the composite polymer systems, which is consistent with the ITC variation in Fig. 3 and follows the relationship between the interfacial potential energy and ITC. However, interfacial potential energy increases while ITC also increases when electric field increases from 1.0 V $Å^{-1}$ to 3.0 V $Å^{-1}$. This might seem surprising but can be explained that the electric field forces push the dissociated ions of IOAs closer to the graphite surfaces than their equilibrium positions, increasing the interfacial potential energy. Consequently, electric fields give greater forces between graphite walls and IOAs, improving the interfacial heat transfer. In previous literature, a pump–probe experiment demonstrated a significant enhancement in thermal transport across gold and PE interfaces by surface modification with SAMs, even though the interfacial adhesion energy increased [63]. To further clarify the heat transfer mechanism of IOAs under the electric fields, vibration density of states was studied in Section 3.4 and ITC is decomposed based on distinct interaction forces at the interface in Section 3.5.

3.4. *Analysis of vibration density of states*

Atomic vibration acts as the heat carrier at the solid–liquid interface, and generally the greater vibration matching between solid and liquid indicates the better interfacial heat transfer [64]. Vibration density of states provides physical insights into the vibrational modes of various materials, which has been used to investigate interfacial heat transfer of solid–liquid interface in many previous studies [50,65], and can be calculated by taking the Fourier transform of the velocity autocorrelation function [66]:

$$G(\omega) = \frac{1}{\sqrt{2\pi}} \int_{-\infty}^{+\infty} e^{-i\omega t} \frac{\langle v(t)v(0)\rangle}{\langle v(0)v(0)\rangle} dt \tag{4}$$

where is $G(\omega)$ the vDOS at an angular frequency ω, $v(t)$ is atom velocity at time t, and the angle bracket denotes the ensemble averaging.

As displayed in Fig. 7(a), electric fields cannot significantly affect the vDOS of PE for graphite-pure polymer systems, which is intuitive because the PE molecules are charged neutral. Hence electric fields should be expected to have little effect on the interfacial heat transfer between graphite walls and PE, which is consistent with the results shown in Fig. 3. As for graphite-composite polymer systems, the electric field affects the distribution and dynamic behaviors of IOAs at the interface, which has been discussed in Section 3.2. Combined with the ITC increase reported in Section 3.1, we then focus on the vDOS of IOAs under electric field. The simulation case of 3.0 V $Å^{-1}$ was taken because IOAs are most significantly affected at this electric field strength.

As the main components, Fig. 7(b) first compares the vDOS of alkyl of DTAB and SDBS backbone with PE. The results show that all three have similar vibration characteristics, which is expected because of the similar structures among them. Then, vDOS of graphite walls, PE, sulfonates of SDBS (SO_3), benzene rings of SDBS, trimethylamines of DTAB ($N(CH_3)_3$), as shown in Fig. 7(c)-(e). In Fig. 7(c), vDOS of sulfonates of SDBS exhibits better vibration matching with graphite than PE at the frequency of 0 – 20.0 THz. As for the benzene rings of SDBS, their vDOS overall overlaps more with graphite because of their similar structure and components (Fig. 7(d)). Especially, the vDOS of the benzene rings of SDBS compensates for the vibration mismatching between the graphite and PE at the frequency of 10.0 – 20.0 THz, 50.0 – 60.0 THz, and around

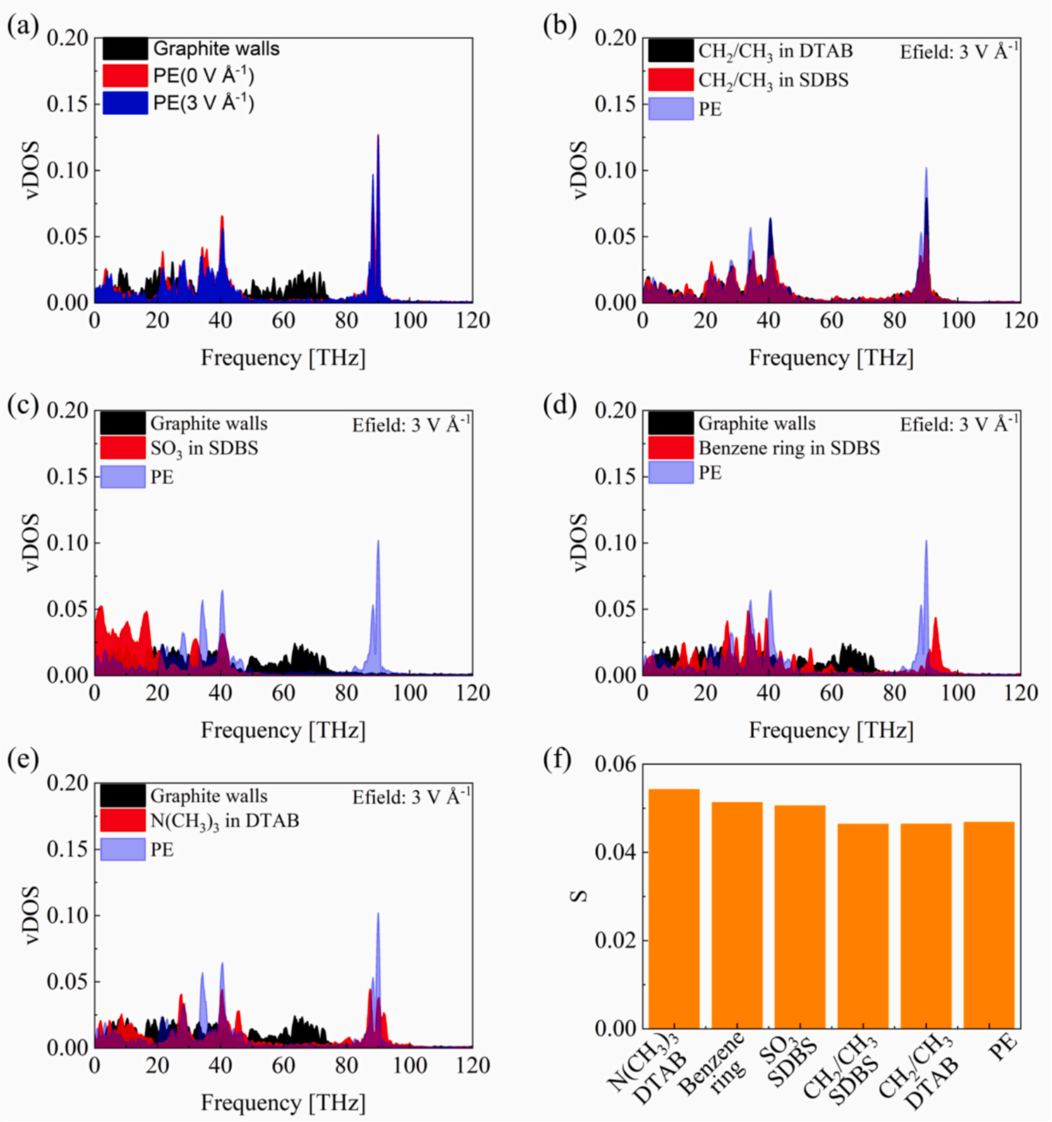

Fig. 7. (a) The vDOS of graphite walls and PE under efield of 0 V Å^{-1} and 3.0 V Å^{-1} for graphite-pure polymer systems. (b) The vDOS of alkyl of DTAB and SDBS backbone and PE under efield of 3.0 V Å^{-1}. The vDOS of graphite walls, PE and (c) sulfonates of SDBS, (d) benzene rings of SDBS, and (e) trimethylamines of DTAB under efield of 3.0 V Å^{-1}. (f) Overlapping factor between graphite walls and trimethylamine of DTAB, benzene ring of SDBS, sulfonate of SDBS, alkyl of DTAB and SDBS backbone, and PE under efield of 3.0 V Å^{-1}.

90.0 THz. Moreover, the vDOS of the benzene rings matches well with that of PE at the frequency of 20.0 – 40.0 THz. Therefore, the benzene rings of SDBS are expected to act as the vibration matching bridge between graphite walls and PE. As shown in Fig. 7(e), the vDOS of trimethylamines of DTAB matches better with graphite than PE at the frequency of 0 – 20.0 THz, and is similar to that of PE at the frequency of 20.0 − 40.0 THz, which should be beneficial to the heat transfer between graphite and PE. All in all, these specific groups in IOAs exhibit better matching of vibration modes than PE, bridge the heat transfer between graphite and PE, and increase ITC. Here, we need to point out that the above analysis is based on the fact that these specific components can stably and persistently aggregate at the interface, which explains why the ITC value does not change too much when the electric field strength is weak shown in Fig. 3.

Finally, we quantitatively assess the degree of the vibration matching by overlapping factor (S) [67]:

$$S = \frac{\int_{-\infty}^{+\infty} G_1(\omega)G_2(\omega)d\omega}{\int_{-\infty}^{+\infty} G_1(\omega)d\omega \int_{-\infty}^{+\infty} G_2(\omega)d\omega} \tag{5}$$

where subscripts “1″ and “2” represent different objects. As shown in Fig. 7(f), compared to the vibration matching between graphite walls and PE, the vDOS matching between graphite walls and trimethylamines of DTAB, benzene rings of SDBS, and sulfonates of SDBS respectively increased by 16.0 %, 9.5 %, and 8.0 %. Meanwhile, the alkyl of DTAB and SDBS backbone and PE exhibit the similar vibration matching degree with the graphite walls. The overlapping factor results are consistent with previous analysis on Fig. 7(b) – (e) in this section. However, the only drawback is that the improvement in vibration matching cannot quantitatively explain the increase in ITC results of Fig. 3, which pushes us the further research in the next section.

3.5. Decomposition of interfacial thermal conductance

According to Eq. (3), ITC decomposition can be obtained by decomposing heat flux between graphite and pure/composite polymers. At the interface between graphite and pure/composite polymers, the total heat flux (J^{total}) is generated through the nonbonded vdW interactions. In this work, the vdW interaction forces are described by the

12–6 Lennard-Jones potential, where the repulsive vdW force switches to the attractive vdW force at the equilibrium point of $2^{1/6}\sigma$. Following the work of Wei et al. [68], we set the $2^{1/6}\sigma$ as the cut-off radius of the 12–6 LJ potential to further decompose J^{total} into an attractive vdW term ($J^{\text{attr.}}$) and a repulsive vdW term ($J^{\text{repl.}}$), as explained in Eq. (6):

$$J^{\text{total}} = J^{\text{attr.}} + J^{\text{repl.}} \tag{6}$$

The heat flux (J) across the interface is calculated via [28,69]:

$$JA = \frac{1}{2}\sum_{m\in\text{GRA}}\sum_{n\in\text{liq.}}\mathbf{F}_{mn}\bullet(\mathbf{v}_m+\mathbf{v}_n) \tag{7}$$

where $\mathbf{F}_{mn}$ is the interaction force between m-th atom of the graphite and n-th atom of the organic liquids,$\mathbf{v}_m$ and $\mathbf{v}_n$ are respectively the velocity vectors of m-th and n-th atoms, and $\bullet$ indicates inner product. Eq. (6) computes the heat flux over a control surface that is positioned at the solid–liquid interface [69–71]. We conducted the calculation of the heat flux via Eq. (6) to acquire J^{total} and $J^{\text{repl.}}$, a $J_z^{\text{attr.}}$ was computed by subtracting $J^{\text{repl.}}$ from J^{total}. After that, substituting the obtained $J^{\text{repl.}}$ and $J^{\text{attr.}}$ into Eq. (3), the corresponding ITC of the repulsive vdW term ($ITC_{\text{repl.}}$) and the attractive term ($ITC_{\text{attr.}}$) were computed. Fig. 8 shows the ITC decomposition results. To estimate the uncertainty of the decomposed ITC results, the total 20 ns of sampling data was broken into 10 blocks to calculate the standard error [49].

As shown in Fig. 8, the thermal energy transport between the graphite and pure/composite polymers is mainly through repulsive vdW interactions and attractive vdW interactions have a negligible effect. As discussed in Fig. 2(a), for the graphite-pure polymer systems, electric fields cannot significantly influence the ITC, and thereby the same is true for the ITC decomposition results of graphite-pure polymer systems. The electric field does not significantly affect the contributions of repulsive and attractive vdW interactions to interfacial heat transfer at the graphite-PE interfaces, shown in Fig. 8(a). Therefore, the rest of this section below focuses on studying the ITC decomposition results of graphite-composite polymer systems shown in Fig. 8(b).

For graphite-composite polymer systems, when the electric field strength is low ($E_{\text{strength}}\leq 0.1$ V Å^{-1}), IOAs cannot cooperate with the electric field to increase ITC. This is because IOAs are not dissociated into two ionic components if the E_{strength} is not high enough, and thereby IOAs still remain as the electrically neutral molecules. As a result, the electric field forces do not drive the electrophoretic migration of IOAs, resulting in the insensitivity of ITC to weak electric field strength. As the electric field strength increases from 0.5 V Å^{-1} to 3.0 V Å^{-1}, ITC sharply increases, predominantly due to increased repulsive vdW interactions that transfer more thermal energy. As discussed earlier, when the electric field strength is larger than 0.1 V Å^{-1}, SDBS molecules begin to dissociate into Na$^+$ and DBS$^-$, and DTAB molecules are dissociated into Br$^-$ and DTA$^+$. Consequently, DBS$^-$ and DTA$^+$ are driven towards the graphite surfaces. As reported by the work of Sun et al. [22], the increased surface ionization can shorten the solid–liquid distance, inducing stronger repulsive vdW interactions to transport more thermal energy. Here, we suggest a mechanism of interfacial thermal transport enhancement due to the cooperation between IOAs and electric fields. First, electric fields promote the dissociation of ionic pairs in SDBS and DTAB molecules (i.e., Na$^+$DBS$^-$ and DTA$^+$Br$^-$). Then, driven by the electric field forces, DBS$^-$ and DTA$^+$ move closer to the graphite surfaces so that the closer solid–liquid distance stimulates stronger repulsive vdW interactions, promoting thermal energy transport. In the result obtained by Han et al. [72], interfacial heat transfer can improve when the pressure on the solid–liquid interface enlarges, which makes the solid and liquid closer. The proposed mechanism in our current work is similar to their findings.

4. Conclusions

In this work, molecular dynamics simulations were conducted to study the interfacial heat transfer between graphite walls and pure/composite polymers under electric fields. Pure polymers were composed from polyethylene (PE), and composite polymers were composed from polyethylene with ionic organic additives (IOAs). Sodium dodecyl benzene sulfonate (SDBS) and dodecyl trimethyl ammonium bromide (DTAB) were chosen as IOAs, respectively consisting of the Na$^+$ and DBS$^-$, and Br$^-$ and DTA$^+$ ionic pairs.

The electric field has little effect on interfacial heat transfer between graphite and PE. At the interface of graphite-composite polymers, ITC hardly varies when the electric field strength is low (≤ 0.1 V Å^{-1}) because PE, SDBS, and DTAB are electrically neutral molecules, and are hardly affected by an external electric field. With stronger electric fields (> 0.1 V Å^{-1}), ITC increases as the electric field strengths. An electric field with higher strength causes the dissociation of IOAs into two independently ionic components, which changes the IOAs distribution at the interface. Driven by the electric field forces, these dissociated ionic components adsorb and move closer to the graphite wall surface, triggering stronger repulsive van der Waals interactions to ultimately improve the interfacial heat transfer. This study explored the novel thermal management strategy of electric fields combined with IOAs to regulate heat transfer, expending the fundamental knowledge of effect of electric fields on heat transfer as well as promoting the development of electronic and energy equipment.

CRediT authorship contribution statement

Haiyi Sun: Conceptualization, Methodology, Software, Visualization, Data curation, Writing – original draft, Writing – review & editing. **Donatas Surblys:** Conceptualization, Methodology, Software, Writing – review & editing. **Taku Ohara:** Conceptualization, Project administration, Writing – review & editing.

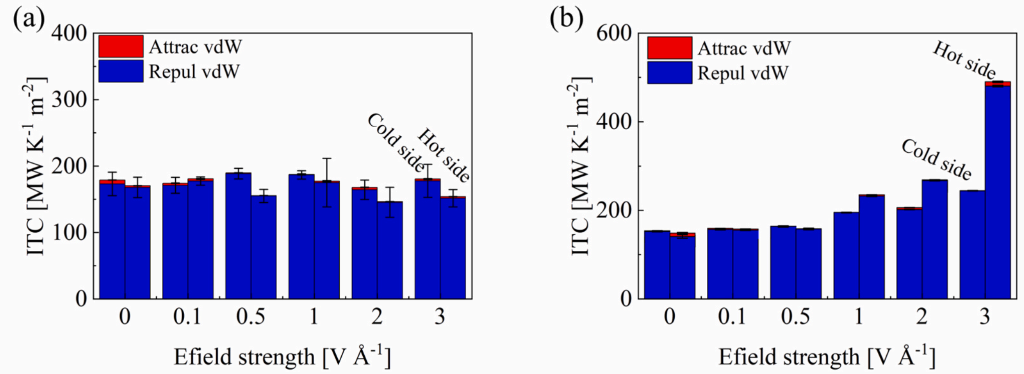

Fig. 8. ITC decomposition for (a) graphite-pure polymer and (b) graphite-composite polymer systems.

Declaration of competing interest

The authors declare that they have no known competing financial interests or personal relationships that could have appeared to influence the work reported in this paper.

Acknowledgements

This work was supported by JSPS KAKENHI JP24K00815. Haiyi Sun acknowledges the support of Research Fellowship for Young Scientists (DC2, Grant No. 24KJ0389) from JSPS. Numerical simulations were performed on the Supercomputer system “AFI-NITY” at the Advanced Fluid Information Research Center, Institute of Fluid Science, Tohoku University.

Appendix A. Supplementary data

Supplementary data to this article can be found online at https://doi.org/10.1016/j.applthermaleng.2025.126803.

Data availability

Data will be made available on request.

References

[1] C. Schüll, H. Frey, Grafting of hyperbranched polymers: from unusual complex polymer topologies to multivalent surface functionalization, Polymer 54 (2013) 5443–5455.
[2] Z. Han, A. Fina, Thermal conductivity of carbon nanotubes and their polymer nanocomposites: a review, Prog. Polym. Sci. 36 (2011) 914–944.
[3] S. Ghosh, I. Calizo, D. Teweldebrhan, E.P. Pokatilov, D.L. Nika, A.A. Balandin, W. Bao, F. Miao, C.N. Lau, Extremely high thermal conductivity of graphene: prospects for thermal management applications in nanoelectronic circuits, Appl. Phys. Lett. 92 (2008).
[4] A.A. Balandin, S. Ghosh, W. Bao, I. Calizo, D. Teweldebrhan, F. Miao, C.N. Lau, Superior thermal conductivity of single-layer graphene, Nano Lett. 8 (2008) 902–907.
[5] K.M.F. Shahil, A.A. Balandin, Graphene–multilayer graphene nanocomposites as highly efficient thermal interface materials, Nano Lett. 12 (2012) 861–867.
[6] A. Yu, P. Ramesh, M.E. Itkis, E. Bekyarova, R.C. Haddon, Graphite nanoplatelet−epoxy composite thermal interface materials, J. Phys. Chem. C 111 (2007) 7565–7569.
[7] J. Xiang, L.T. Drzal, Investigation of exfoliated graphite nanoplatelets (xGnP) in improving thermal conductivity of paraffin wax-based phase change material, Sol. Energy Mater. Sol. Cells 95 (2011) 1811–1818.
[8] C.W. Nan, R. Birringer, D.R. Clarke, H. Gleiter, Effective thermal conductivity of particulate composites with interfacial thermal resistance, J. Appl. Phys. 81 (1997) 6692–6699.
[9] S.Y. Yang, W.N. Lin, Y.L. Huang, H.W. Tien, J.Y. Wang, C.C.M. Ma, S.M. Li, Y. S. Wang, Synergetic effects of graphene platelets and carbon nanotubes on the mechanical and thermal properties of epoxy composites, Carbon 49 (2011) 793–803.
[10] W. Yu, H. Xie, L. Chen, Z. Zhu, J. Zhao, Z. Zhang, Graphene based silicone thermal greases, Phys. Lett. A 378 (2014) 207–211.
[11] X. Feng, M. Ouyang, X. Liu, L. Lu, Y. Xia, X. He, Thermal runaway mechanism of lithium ion battery for electric vehicles: a review, Energy Storage Mater. 10 (2018) 246–267.
[12] S. Ganguli, A.K. Roy, D.P. Anderson, Improved thermal conductivity for chemically functionalized exfoliated graphite/epoxy composites, Carbon 46 (2008) 806–817.
[13] D. Konatham, A. Striolo, Thermal boundary resistance at the graphene-oil interface, Appl. Phys. Lett. 95 (2009).
[14] M. Wang, D. Galpaya, Z.B. Lai, Y. Xu, C. Yan, Surface functionalization on the thermal conductivity of graphene–polymer nanocomposites, Int. J. Smart Nano Mater. 5 (2014) 123–132.
[15] Y. Wang, H.F. Zhan, Y. Xiang, C. Yang, C.M. Wang, Y.Y. Zhang, Effect of covalent functionalization on thermal transport across graphene-polymer interfaces, J. Phys. Chem. C 119 (2015) 12731–12738.
[16] Y. Wang, C. Yang, Y.W. Mai, Y. Zhang, Effect of non-covalent functionalisation on thermal and mechanical properties of graphene-polymer nanocomposites, Carbon 102 (2016) 311–318.
[17] A.C. Aragones, N.L. Haworth, N. Darwish, S. Ciampi, N.J. Bloomfield, G. G. Wallace, I. Diez-Perez, M.L. Coote, Electrostatic catalysis of a Diels–Alder reaction, Nature 531 (2016) 88–91.
[18] N. Balke, S. Jesse, B. Carmichael, M.B. Okatan, I.I. Kravchenko, S.V. Kalinin, A. Tselev, Quantification of in-contact probe-sample electrostatic forces with dynamic atomic force microscopy, Nanotechnology 28 (2017) 65704.
[19] G. Wang, Z. Zhang, R. Wang, Z. Zhu, A review on heat transfer of nanofluids by applied electric field or magnetic field, Nanomaterials 10 (2020) 2386.
[20] S.A. Zonouzi, H. Aminfar, M. Mohammadpourfard, A review on effects of magnetic fields and electric fields on boiling heat transfer and CHF, Appl. Therm. Eng. 151 (2019) 11–25.
[21] D. Li, H. Yang, L. Li, P. Yang, Numerical investigation of thermal conductivity of Cu/graphene/Cu interface, Appl. Phys. Lett. 123 (2023).
[22] H. Yang, Y. Tang, P. Yang, Factors influencing thermal transport across graphene/metal interfaces with van der Waals interactions, Nanoscale 11 (2019) 14155–14163.
[23] H. Yang, S. Gao, Y. Pan, P. Yang, Manipulating heat transfer at graphene/silicon interface with nitrogen doping, Int. Commun. Heat Mass Transf. 155 (2024) 107521.
[24] H. Yang, Y. Shen, L. Li, Y. Pan, P. Yang, Surface modification to induce efficient heat transfer at graphene/silicon heterointerface, Appl. Therm. Eng. 238 (2024) 121913.
[25] Y. Ma, Z. Zhang, J. Chen, K. Sääskilahti, S. Volz, J. Chen, Ordered water layers by interfacial charge decoration leading to an ultra-low Kapitza resistance between graphene and water, Carbon 135 (2018) 263–269.
[26] J. Song, M. An, Y. Guo, D. Chen, B. Yao, H. Chen, G. Zhang, Electrically regulated thermal conductivity of aramid polymer systems, Appl. Phys. Lett. 124 (2024).
[27] Y. Guo, D. Surblys, H. Matsubara, T. Ohara, A molecular dynamics study of the effect of functional groups and side chain on adsorption of alcoholic surfactant and interfacial thermal transport, J. Mol. Liq. 335 (2021) 116243.
[28] Y. Guo, D. Surblys, H. Matsubara, Y. Kawagoe, T. Ohara, Molecular dynamics study on the effect of long-chain surfactant adsorption on interfacial heat transfer between a polymer liquid and silica surface, J. Phys. Chem. C 124 (2020) 27558–27570.
[29] H. Wu, J. Gao, Y. Xiong, Q. Zhu, Y. Yue, Tuning thermal conductance of graphene-polyethylene composites via graphene inclination and curvature, Int. J. Heat Mass Transf. 178 (2021) 121634.
[30] S. Güryel, M. Walker, P. Geerlings, F. De Proft, M.R. Wilson, Molecular dynamics simulations of the structure and the morphology of graphene/polymer nanocomposites, Phys. Chem. Chem. Phys. 19 (2017) 12959–12969.
[31] S. Tian, D. Huang, Z. Xu, S. Wu, T. Luo, G. Xiong, Enhanced thermal transport across the interface between charged graphene and poly (ethylene oxide) by non-covalent functionalization, Int. J. Heat Mass Transf. 183 (2022) 122188.
[32] A.P. Thompson, H.M. Aktulga, R. Berger, D.S. Bolintineanu, W.M. Brown, P. S. Crozier, P.J. in't Veld, A. Kohlmeyer, S.G. Moore, T.D. Nguyen, LAMMPS-a flexible simulation tool for particle-based materials modeling at the atomic, meso, and continuum scales, Comput. Phys. Commun. 271 (2022) 108171.
[33] Verlet, A time integration algorithm for dynamics, Phys. Rev 165 (1967) 67–94.
[34] A. Stukowski, Visualization and analysis of atomistic simulation data with OVITO–the open visualization tool, Model. Simul. Mater. Sci. Eng. 18 (2009) 15012.
[35] J. Tersoff, Modeling solid-state chemistry: Interatomic potentials for multicomponent systems, Phys. Rev. B 39 (1989) 5566.
[36] L.A. Girifalco, M. Hodak, R.S. Lee, Carbon nanotubes, buckyballs, ropes, and a universal graphitic potential, Phys. Rev. B 62 (2000) 13104.
[37] K.P. Jensen, W.L. Jorgensen, Halide, ammonium, and alkali metal ion parameters for modeling aqueous solutions, J. Chem. Theory Comput. 2 (2006) 1499–1509.
[38] C.J. Fennell, A. Bizjak, V. Vlachy, K.A. Dill, S. Sarupria, S. Rajamani, S. Garde, Ion pairing in molecular simulations of aqueous alkali halide solutions, J. Phys. Chem. B 113 (2009) 14837–14838.
[39] L.S. Dodda, I. Cabeza de Vaca, J. Tirado-Rives, W.L. Jorgensen, LigParGen web server: an automatic OPLS-AA parameter generator for organic ligands, Nucleic Acids Res. 45 (2017) W331–W336.
[40] R. Yang, D. Chen, W. Zheng, T. Miao, F. Liu, T. Wang, H. Chen, T. Cheng, Theoretical insight into the effect of steam temperature on heavy oil/steam interface behaviors using molecular dynamics simulation, J. Therm. Sci. 32 (2023) 2179–2195.
[41] S.A. Shavalier, J.D. Gezelter, Thermal TRANSPORT THROUGH CTAB-and MTAB-functionalized gold interfaces using molecular dynamics simulations, J. Chem. Inf. Model. (2025).
[42] R.W. Hockney, J.W. Eastwood, Computer Simulation Using Particles, Adam Hilger, New York, 1989.
[43] I.C. Yeh, M.L. Berkowitz, Ewald summation for systems with slab geometry, J. Chem. Phys. 111 (1999) 3155–3162.
[44] M.E. Tuckerman, J. Alejandre, R. López-Rendón, A.L. Jochim, G.J. Martyna, A Liouville-operator derived measure-preserving integrator for molecular dynamics simulations in the isothermal–isobaric ensemble, J. Phys. A. Math. Gen. 39 (2006) 5629.
[45] G.J. Martyna, D.J. Tobias, M.L. Klein, Constant pressure molecular dynamics algorithms, J. Chem. Phys. 101 (1994) 4177–4189.
[46] S.C. Lin, K. Banerjee, Cool chips: opportunities and implications for power and thermal management, IEEE Trans. Electron Devices 55 (2007) 245–255.
[47] M.A.P. Pertijs, K.A.A. Makinwa, J.H. Huijsing, A CMOS smart temperature sensor with a 3 inaccuracy of 0.1 ℃ from 55 ℃ to 125 ℃, IEEE J. Solid-State Circuits 40 (2005) 2805–2815.
[48] B. Xu, J. Lee, D. Kwon, L. Kong, M. Pecht, Mitigation strategies for Li-ion battery thermal runaway: a review, Renew. Sustain. Energy Rev. 150 (2021) 111437.
[49] D.G. Altman, J.M. Bland, Standard deviations and standard errors, BMJ 331 (2005) 903.
[50] H. Sun, D. Surblys, H. Matsubara, T. Ohara, Molecular dynamics study on the role of hydrogen bonds and interfacial heat transfer between diverse silica surfaces and organic liquids, Int. J. Heat Mass Transf. 208 (2023) 124091.

[51] F. Carman, J.P. Ewen, F. Bresme, B. Wu, D. Dini, Molecular simulations of thermal transport across iron oxide–hydrocarbon interfaces, ACS Appl. Mater. Interfaces 16 (2024) 59452–59467.
[52] J.D. Olarte-Plata, F. Bresme, Thermal conductance of the water–gold interface: the impact of the treatment of surface polarization in non-equilibrium molecular simulations, J. Chem. Phys. 156 (2022).
[53] H. Ettouney, H. El-Dessouky, A. Al-Ali, Heat transfer during phase change of paraffin wax stored in spherical shells, J. Sol. Energy Eng. 127 (2005) 357–365.
[54] A. Sarı, A. Karaipekli, Thermal conductivity and latent heat thermal energy storage characteristics of paraffin/expanded graphite composite as phase change material, Appl. Therm. Eng. 27 (2007) 1271–1277.
[55] H. Fan, M. Wang, D. Han, J. Zhang, J. Zhang, X. Wang, Enhancement of interfacial thermal transport between metal and organic semiconductor using self-assembled monolayers with different terminal groups, J. Phys. Chem. C 124 (2020) 16748–16757.
[56] J. Dominikowska, M. Palusiak, Tuning aromaticity of para-substituted benzene derivatives with an external electric field, ChemPhysChem 19 (2018) 590–595.
[57] J. Björk, F. Hanke, C.-A. Palma, P. Samori, M. Cecchini, M. Persson, Adsorption of aromatic and anti-aromatic systems on graphene through π−π stacking, J. Phys. Chem. Lett. 1 (2010) 3407–3412.
[58] B. Shen, W. Zhai, C. Chen, D. Lu, J. Wang, W. Zheng, Melt blending in situ enhances the interaction between polystyrene and graphene through π–π stacking, ACS Appl. Mater. Interfaces 3 (2011) 3103–3109.
[59] H. Sun, D. Surblys, S. Cheng, T. Ohara, Molecular dynamics study on the effect of surface ionization on the interfacial heat transfer between silica and water, Appl. Therm. Eng. 244 (2024) 122762.
[60] T. Vallier, R.B. Nuernberg, S. Issa, J.L. Ferrandis, L. Stievano, B. Ameduri, V. Lapinte, L. Monconduit, Understanding Na^+ diffusion, physicochemical behavior, and electrochemical performance of a gel polymer electrolyte, ACS Appl. Mater. Interfaces 16 (2024) 29077–29086.
[61] R. Flack, A. Aixalà-Perelló, A. Pedico, K. Saadi, A. Lamberti, D. Zitoun, Permselectivity and ionic conductivity study of Na^+ and Br^- ions in graphene oxide-based membranes for redox flow batteries, Membranes 13 (2023) 695.
[62] T. Zhang, A.R. Gans-Forrest, E. Lee, X. Zhang, C. Qu, Y. Pang, F. Sun, T. Luo, Role of hydrogen bonds in thermal transport across hard/soft material interfaces, ACS Appl. Mater. Interfaces 8 (2016) 33326–33334.
[63] F. Sun, T. Zhang, M.M. Jobbins, Z. Guo, X. Zhang, Z. Zheng, D. Tang, S. Ptasinska, T. Luo, Molecular bridge enables anomalous enhancement in thermal transport across hard-soft material interfaces, Adv. Mater. 26 (2014) 6093–6099.
[64] Y. Zhao, G. Kikugawa, Y. Kawagoe, K. Shirasu, T. Okabe, Molecular-scale investigation on relationship between thermal conductivity and the structure of crosslinked epoxy resin, Int. J. Heat Mass Transf. 198 (2022) 123429.
[65] Z. Xu, D. Huang, T. Luo, Molecular-level understanding of efficient thermal transport across the silica–water interface, J. Phys. Chem. C 125 (2021) 24115–24125.
[66] D. Han, X. Wang, W. Ding, Y. Chen, J. Zhang, G. Xin, L. Cheng, Phonon thermal conduction in a graphene–C_3N heterobilayer using molecular dynamics simulations, Nanotechnology 30 (2018) 75403.
[67] H. Sun, Z. Liu, G. Xin, Q. Xin, J. Zhang, B.Y. Cao, X. Wang, Thermal and flow characterization in nanochannels with tunable surface wettability: a comprehensive molecular dynamics study, Numer. Heat Transf. Part A Appl. 78 (2020) 231–251.
[68] X. Wei, T. Luo, Role of ionization in thermal transport of solid polyelectrolytes, J. Phys. Chem. C 123 (2019) 12659–12665.
[69] T. Ohara, Contribution of intermolecular energy transfer to heat conduction in a simple liquid, J. Chem. Phys. 111 (1999) 9667–9672.
[70] H. Matsubara, G. Kikugawa, T. Bessho, S. Yamashita, T. Ohara, Molecular dynamics study on the role of hydroxyl groups in heat conduction in liquid alcohols, Int. J. Heat Mass Transf. 108 (2017) 749–759.
[71] D. Surblys, H. Matsubara, G. Kikugawa, T. Ohara, Application of atomic stress to compute heat flux via molecular dynamics for systems with many-body interactions, Phys. Rev. E 99 (2019) 51301.
[72] H. Han, S. Mérabia, F. Müller-Plathe, Thermal transport at solid–liquid interfaces: high pressure facilitates heat flow through nonlocal liquid structuring, J. Phys. Chem. Lett. 8 (2017) 1946–1951.